



## Chapter 2

# Physics of Liquid Argon Time Projection Chambers

The Liquid Argon Time Projection Chamber (LArTPC) stands as a high precision detector in neutrino physics. In contrast to liquid scintillator neutrino experiments, LArTPCs collect both light and charge thereby providing a superior granularity for imaging neutrino interactions. The detector concept was first proposed in 1977 by Rubbia [1], bringing together the time projection chamber technology developed by Nygren [2, 3] and the liquid argon ionisation chamber developed by Willis and Radeka [4]. LArTPC provides excellent spatial, calorimetry and timing resolution while enabling a high neutrino interaction rate. Thus, this novel technology remains the primary choice for many neutrino experiments at Fermilab.

The following chapter will delve into the operating principles of a LArTPC, which is the detection technology employed by the Short-Baseline Near Detector to be discussed in the forthcoming Chapter 3. Sec. 2.1 provides an overview of the design of a LArTPC and the choice of liquid argon. In Sec. 2.2, a comprehensive discussion is presented on particle interactions with the liquid argon and the production of ionisation electrons and scintillation photons, which are the observables of a LArTPC. Following that, Sec. 2.3 outlines the propagation of the resultant electrons and photons through the liquid argon medium. Sec. 2.4 provides an insight into the detection mechanism of the ionisation electrons and scintillation photons using wire planes and novel optical detection technologies respectively. Finally, Sec. 2.5 concludes the chapter with some remarks.

## 2.1 Overview of LArTPCs

The Liquid Argon Time Projection Chamber (LArTPC) is the technology of choice for Fermilab's neutrino program, due to its ability to facilitate a high rate of neutrino interactions while maintaining an exceptional spatial, energy, and timing resolution. Moreover, the abundance and low cost of argon are ideal for scaling detectors to a large target mass, reaching up to tens of kilotons of liquid argon. Notably, the Short-Baseline Neutrino (SBN) programme [5] comprises three LArTPC experiments each of size in the hundreds of tons, located along the Booster Neutrino Beam (BNB): the Short-Baseline Near Detector (SBND) [6], MicroBooNE [7], and ICARUS [8]. This novel technology will also be utilised at the upcoming long baseline Deep Underground Neutrino Experiment (DUNE), of which two of the four far modules are LArTPCs, each with a volume of 17 kilotons [9].

Fig. 2.1 shows a diagram illustrating a general LArTPC. The TPC comprises a volume of LAr with a uniform electric field provided by a surrounding field cage, which is not shown in the diagram. To the right of the TPC is a cathode grounded at a high negative voltage and to the left is the anode plane assembly, and thus the resulting electric field direction is from left to right. The anode plane assembly is made up of three wire planes oriented at different angles, of which the diagram here shows three planes at the angle of  $0^\circ$  and  $\pm 60^\circ$  to the vertical. Behind the wire planes is the Photon Detection System (PDS) comprising 9 PhotoMultiplier Tubes (PMTs).

The centre of the LArTPC in Fig. 2.1 also depicts an example interaction of an incoming neutrino scattering off an argon nucleus, shown as the dashed line since the neutral track of the neutrino is unobservable by the detector. Charged particles resulting from the neutrino interaction ionise and excite argon atoms as they traverse through the detector medium, producing ionisation electrons and scintillation photons in the process as shown by the solid lines. Ionisation electrons drift towards the anode in the opposite direction of the electric field. Upon arrival at the anode, ionisation electrons induce signals on the two inner wire planes and are collected on the outermost wire plane. The combination of signals from the three planes results in a high granularity three-dimensional image of the charged particle path. Moreover, since the wire planes are transparent to scintillation photons, the photons drift past the wire planes and are detected by the PDS. Scintillation photons provide additional information about the deposited energy and precise timing information of the neutrino interaction.

Liquid argon makes an excellent medium for TPCs in neutrino experiments. Given that liquid argon has a reasonably high density of  $1.39 \text{ g}\cdot\text{cm}^{-3}$  and an atomic mass of 40, it enables

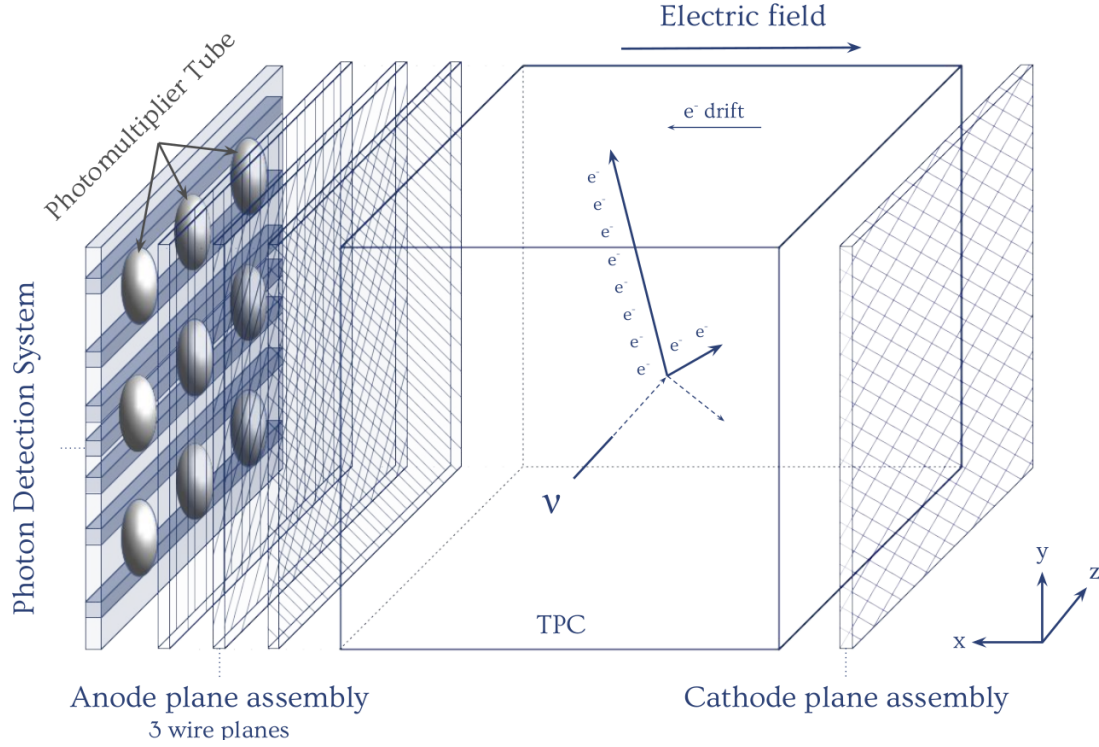


**Fig. 2.1** Diagram illustrating the operating principles of a LArTPC [10].

a high rate of neutrino interactions since the probability of neutrino interactions increases with the number of nucleons in the detector volume. Furthermore, given that argon is a noble element, most of the energy deposited by particles traversing through the medium is used for ionising and exciting atoms, producing ionisation electrons and scintillation photons in the processes. This maximises the efficiency of energy transfer into observable signals as well as enables a low energy threshold for detection in the order of  $\mathcal{O}(10)$  MeV. In addition to argon being an abundant and cheap material for scaling the detector target mass, recent technology advancements in purifying liquid argon have resulted in a stable and pure liquid argon condition for LArTPC operation. This ensures that observable signals from electrons and photons can traverse the drift distance towards detection without being captured by contaminants [11]. Consequently, liquid argon continues to stand out as an advantageous target material for neutrino experiments.

## 2.2 Particle Interactions in Liquid Argon

Particle interactions in liquid argon and the production of ionisation electrons and scintillation photons as observable signals are discussed in the following section. Sec. 2.2.1 provides a description of the energy loss of charged particles traversing liquid argon and producing ionisation electrons. Following that, Sec. 2.2.2 details the production mechanism of scintillation photons via excitation and recombination. Finally, Sec. 2.2.3 goes into more detail of the physics of recombination that determines the yield of ionisation electrons and scintillation photons.

### 2.2.1 Ionisation Electrons

Charged particles traversing a medium, such as liquid argon, undergo energy loss via ionisation, producing electrons. The typical energy loss profile is illustrated in Fig. 2.2, specifically for a muon traversing in a copper medium; however, the underlying principle applies to liquid argon. The plot depicts the stopping power, which is the energy loss per unit length divided by the density of the target medium, against the momentum of the traversing particle [12]. Heavy particles such as muons, pions, and protons, experience energy loss in liquid argon described by the Bethe-Bloch formalism [12]. For lighter and highly relativistic particles, such as  $> 100$  MeV electrons in liquid argon, the primary mechanism for energy loss is through radiative effects.

Muons, pions and protons interact electromagnetically with argon atoms as they propagate through liquid argon primarily via ionisation, freeing electrons along their trajectories. These straight-line trajectories are referred to as *tracks*. The trajectories can also be deflected by many small angle scattering, a phenomenon known as Multiple Coulomb Scattering due to charged particles Coulomb scattering from nuclei [12]. Within the momentum range of 1–100 MeV, the energy deposited per unit length via ionisation  $dE/dx$  remains generally constant, often referred to as the Minimum Ionising Particle (MIP). In this MIP region, the distribution of  $dE/dx$  is described by a Landau-Gaussian convolution [12]. When the particle comes to a stop, the deposited energy increases, forming the Bragg peak. The energy loss profile described here is dependent on the mass of the traversing particle, making it a valuable tool for Particle IDentification (PID) [13]. This method is the most effective for protons separation from muons and pions as protons are significantly heavier.

Electrons with energy above the critical energy, which is the point losses due to ionisation are equal to losses from radiation, deposit energy via radiative effects. The critical

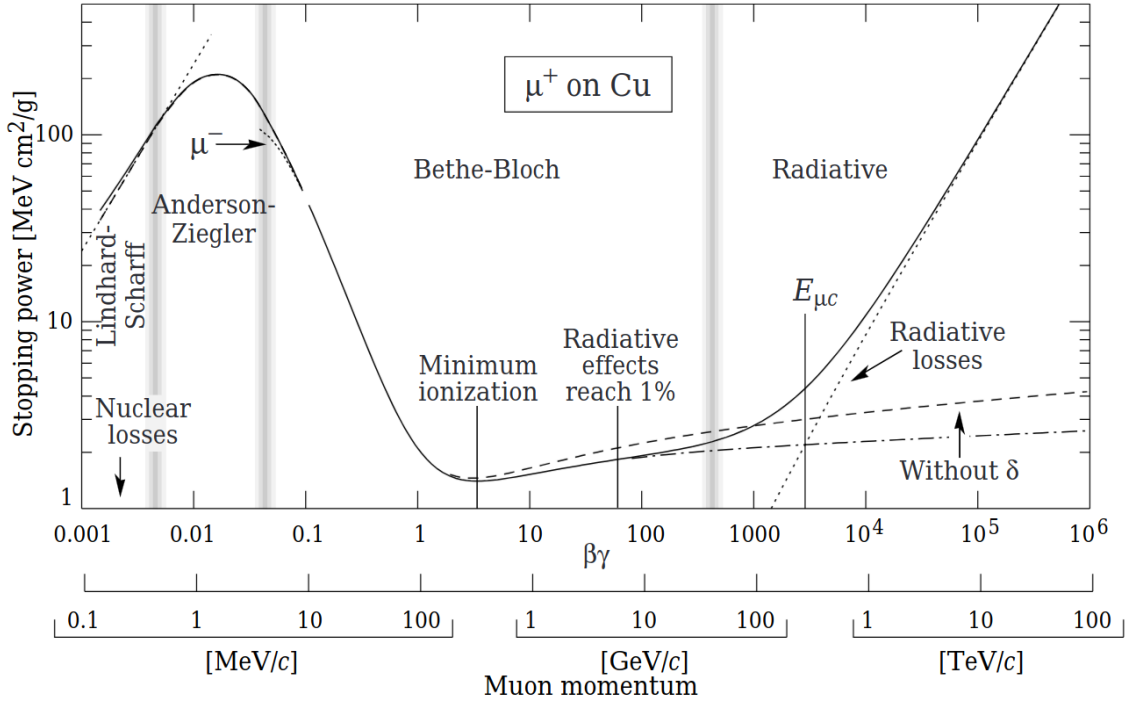


**Fig. 2.2** Example of particle energy loss in matter for a muon traversing a copper medium [12].

energy for electrons in liquid argon is 39 MeV [14]. This process typically results in cones of electromagnetic activities, commonly referred to as *showers*. In the energy range relevant in a LArTPC, typically between 100–1000 MeV, showers deposit energy over a distance of  $\sim 1$  m, and the shower length is logarithmic in energy. For electrons resulting from a muon decay with an energy of  $\sim 50$  MeV, they neither resemble an ionisation track nor an electromagnetic shower. Instead, they result in a short linear segment of ionisation followed by a few clumps of deposited charge in the energy range of 1–10 MeV. This unique energy deposition of electrons is referred to as a *Michel electrons* and is often used by LArTPC experiments for energy calibration and identifying muons [15].

Photons deposit energy via Compton scattering and  $e^+e^-$  pair production, also producing electromagnetic showers similar to energetic electrons. Fig. 2.3 shows the mean free path of photons in liquid argon as a function of the photon energy for the two modes, Compton scattering by the solid blue line and pair production by the solid red line. At the low energy range  $< 50$  MeV, the main interaction mode is via Compton scattering while at the high energy range  $> 50$  MeV, pair production becomes the dominant effect. The mean free path for a photon for pair production is defined as  $9/7$  of the radiation length of an electron and it is plotted as the solid cyan line at 18.1 cm. In the photon energy range of

100–1000 MeV relevant for LArTPCs, it can be seen that photons typically travel 20–30 cm without causing ionisation. This creates a gap between the interaction vertex and the start of the shower, known as the *conversion gap*. Both the energy loss profiles and the conversion gaps can be utilised to distinguish between electrons and photons.

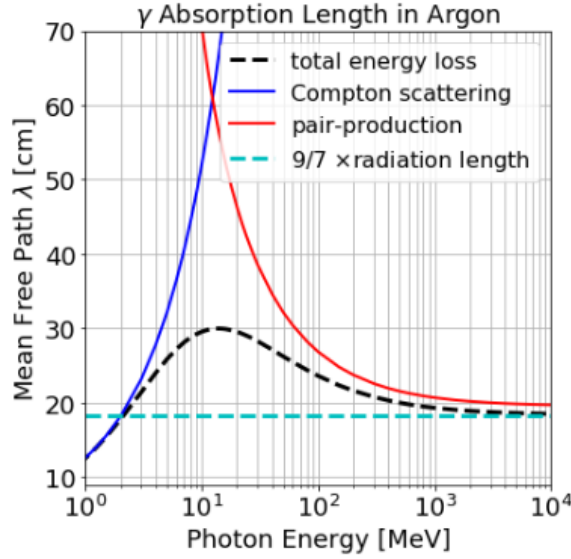


**Fig. 2.3** Plot showing the mean free path of photons traversing in liquid argon as a function of their energies [14].

Fig. 2.4 shows an event display of a simulated charged current  $\nu_\mu$  interaction containing a muon, a proton and a neutral pion in the final state. The colour scale corresponds to the magnitude of the energy deposition, where the colour green is lower in ionisation and the colour red is higher in ionisation. The muon results in a long minimum ionising track whilst the proton results in a short energetic stub, demonstrating the distinct difference between the energy loss profile of a muon and a proton. Moreover, as the muon comes to a stop, the colour scale changes from green to red, which indicates the increase in energy forming the Bragg peak. At the end of the muon track, it decays into a Michel electron that resembles a short linear segment low in energies. On the other hand, the neutral pion decays into two photons, which both undergo pair production producing electromagnetic showers. The photon showers are detached from the interaction vertex where both muon and proton tracks begin. This is the conversion gap feature unique to a photon shower.

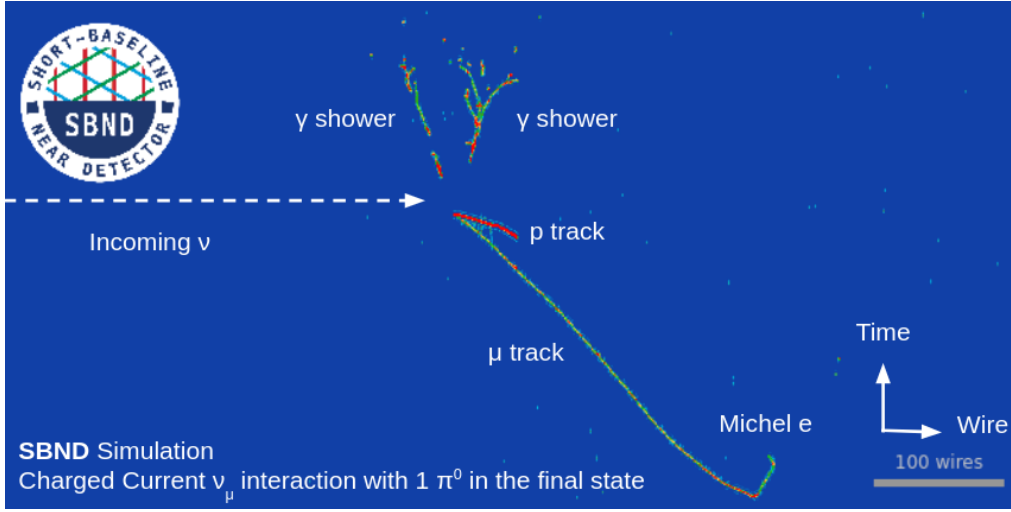


**Fig. 2.4** Event display showing a simulated charged current  $\nu_\mu$  interaction containing a muon, a proton and a neutral pion in the final state.

### 2.2.2 Scintillation Photons

Charged particles traversing liquid argon also produce scintillation photons, through two different processes that result in an argon excimer  $Ar_2^*$  as shown in Fig. 2.5. The first process is known as recombination, denoted by the arrows labelled *ionize* and *recombine*. Ionisation in liquid argon produces a free electron and an argon ion  $Ar^+$ . The electron can either escape and drift towards the anode for detection, or recombine with an argon compound ion  $Ar_2^+$ , forming an argon excimer. The second process is known as a self-trapped exciton, denoted by the arrow labelled *excite*. This begins when the charged particle does not have sufficient energy for ionisation, instead it excites the argon atom upon collision. The excited argon atom  $Ar^*$  self-traps with another argon atom  $Ar$ , forming an argon excimer. The resulting argon excimer from both processes is short-lived and undergoes radiative decay into two ground-state argon atoms. This produces scintillation photons with a wavelength of 128 nm in the Vacuum Ultraviolet (VUV) range [16].

The timing constant of the radiative decay depends on the excitation state of the argon excimer. This can be either a singlet state where the excited electron has the same spin as in the ground state or the triplet state where the excited electron has the same spin as another unpaired electron. The singlet state has a shorter mean lifetime with a decay constant  $\tau_1 \approx 6-7$  ns, while the triplet state has a longer mean lifetime with a decay constant  $\tau_3 \approx 1.5-1.6$   $\mu$ s [17]. These are referred to as the prompt and or late components, respectively.



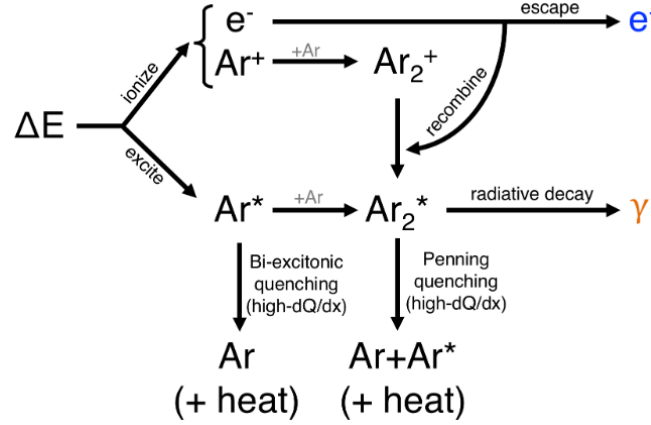


**Fig. 2.5** Diagram illustrating the production of ionisation electrons and scintillation photons from energy deposition processes in liquid argon [16].

The time-dependent probability of light emission in pure liquid argon is modelled as

$$I(t) = \frac{A_1}{\tau_1} \exp\left(-\frac{t}{\tau_1}\right) + \frac{A_3}{\tau_3} \exp\left(-\frac{t}{\tau_3}\right) \quad (2.1)$$

where  $A_1$  and  $A_3$  are the decay amplitudes of the singlet and triplet state.

Liquid argon serves as an excellent medium for producing scintillation photons, such that the light yield is as high as  $\sim 40,000$  photons per MeV of deposited energy in the absence of an electric field [18]. In a typical electric field at 500 V/cm, as configured in SBND, the light yield decreases to  $\sim 20,000$  photons per MeV of deposited energy due to free electrons being drifted before recombination can occur [19]. Furthermore, high ionisation density may lead to non-radiative quenching effects [16]. Contaminants in liquid argon, such as oxygen and nitrogen, can absorb energy from argon excitons and excimers, without emitting any photons.

### 2.2.3 Recombination

The electron-ion recombination, as depicted by the arrow labelled *recombine* in Fig. 2.5, is a key physics process affecting the yield of ionisation electrons and scintillation photons. Recombination occurs almost immediately within 1-2 ns following the ionisation process. The recombination factor  $R$  is defined as the survival probability of electrons that do not recombine. Fig. 2.6 shows a comparison of various  $R$  models with a non-linear dependence on the energy density  $dE/dx$  for liquid argon at an electric field of 500 V/cm [20]. The

Birks model, shown by the solid blue line, has been disfavoured due to spurious values at high charge density. The Box model, shown by the solid red line, is based on the columnar theory around the charge deposition and can resolve the issue suffered by the Birks model. It has been recently modified for better agreement with the Birks model at low charge density which accounts for the presence of an electric field and local ionisation density. The modified Box model, as shown by the dotted red line, also contains experimentally derived parameters measured by the ArgoNeuT experiment [20].

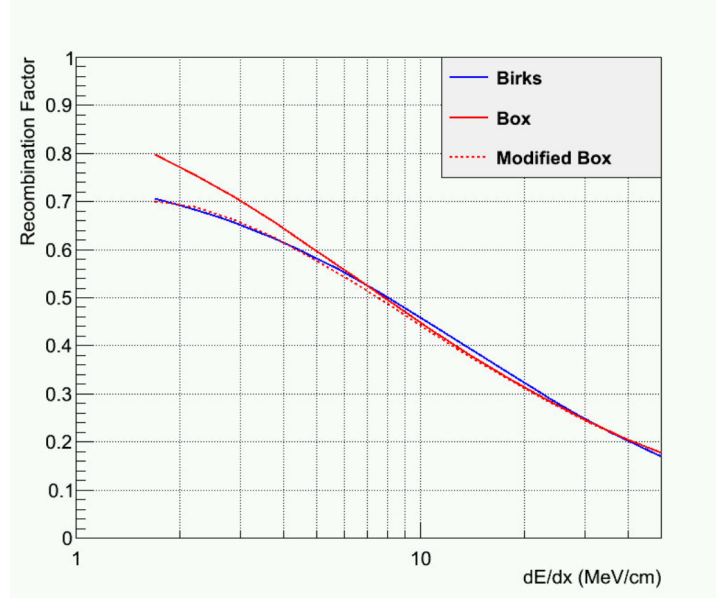


**Fig. 2.6** Plot showing the recombination factor in liquid argon as a function of the deposited energy density for an electric field of 500 V/cm [20].

The dependence of recombination on the electric field leads to an anti-correlation between the charge and light yield  $Q$  and  $L$  respectively, such that [20]

$$Q = N_i R \quad (2.2)$$

$$L = N_{ex} + N_i(1 - R) \quad (2.3)$$

where  $N_i$  is the number of electron-ion pairs and  $N_{ex}$  is the number of argon excitons. Fig. 2.7 illustrates the anti-correlation as a function of the electric field strength for various noble elements, of which argon is shown as dashed lines. A stronger electric field results in a higher number of ionisation electrons being separated from the argon ions and drifting towards the anode for detection before recombination can occur, thus increasing the charge yield. Conversely, scintillation photons are produced in the recombination process. In the presence of an electric field, recombination decreases, leading to a reduction in light

yield. Furthermore, the recombination factor can be influenced at a local scale due to ionisation density resulting from interacting particles. The SBND detector operates with an electric field of 500 V/cm, a region where the energy deposition to ionisation electrons and scintillation electrons are approximately equal as can be seen in Fig. 2.7. The impact of recombination on the observed physics will be further discussed in Chapter 7, Sec. 7.2.

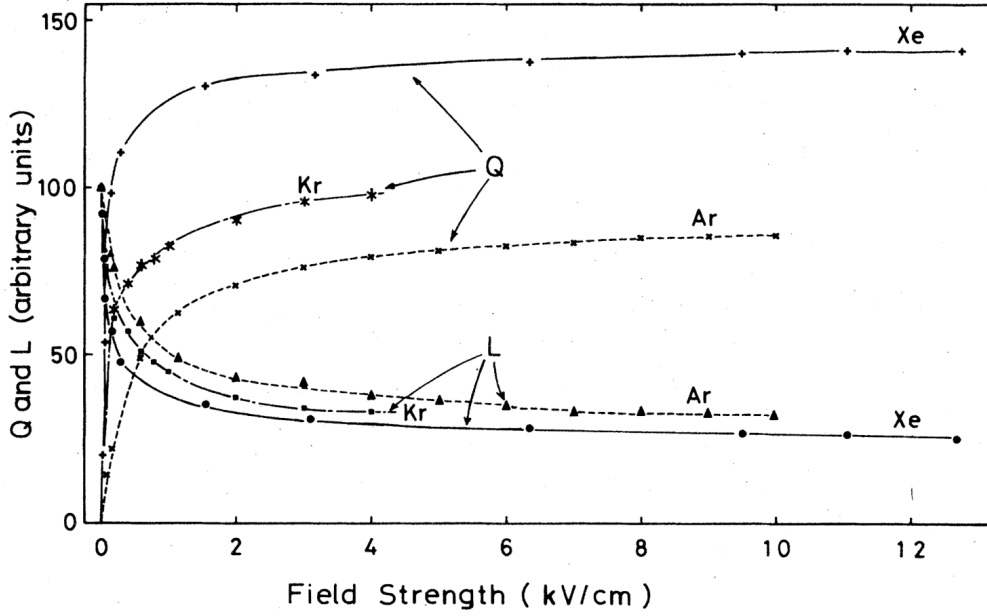


**Fig. 2.7** Plot showing the charge yield  $Q$  and light yield  $L$  anti-correlation as a function of the electric field strength [21].

## 2.3 Particle Propagation in Liquid Argon

The following section provides a description of the transportation of ionisation electrons and scintillation photons through the liquid argon medium. Sec. 2.3.1 covers the details of different physics processes that electrons experience as they drift towards the anode, including diffusion, attenuation and the space charge effect. On the other hand, a discussion on the propagation of photons is presented in Sec. 2.3.2, detailing the process of Rayleigh scattering, absorption and wavelength shifting.

### 2.3.1 Electron Drift

Ionisation electrons that do not recombine drift towards the anode under the effect of an electric field. In a typical LArTPC with an electric field of 500 V/cm and a temperature of

### 2.3 Particle Propagation in Liquid Argon

---

87 K, the drift velocity of electrons is approximately  $0.16 \text{ cm}/\mu\text{s}$  [22]. As the electrons drift, they undergo diffusion, causing perturbations in their trajectories due to various effects. For example, it can be due to inelastic collisions with argon atoms. Diffusion causes the shape of a cloud of electrons produced in a point-like energy deposition to grow in volume while drifting. The effects increase with the drift distance, smearing both spatial and temporal resolutions.

Diffusion is parameterised in both the longitudinal and the transverse direction, which are parallel and perpendicular to the drift direction respectively. Longitudinal diffusion affects the temporal resolution, as individual electrons arrive at the wire either earlier or later relative to the electron cloud moving at the average drift velocity. The temporal smearing due to the longitudinal diffusion can be approximated as [23]

$$\sigma_L \approx \sqrt{\frac{2D_L}{v_d^2} t} \quad (2.4)$$

where  $D_L \text{ (cm}^2/\text{s)}$  is the longitudinal diffusion,  $v_d \text{ (cm/s)}$  is the drift velocity and  $t \text{ (s)}$  is the drift time. On the other hand, transverse diffusion broadens the cross section of the electron cloud arriving at the original wire, causing electrons to migrate to neighbouring wires. The spatial smearing due to the transverse diffusion can be approximated as [24]

$$\sigma_T \approx \sqrt{2 \cdot D_T \cdot t} \quad (2.5)$$

where  $D_T \text{ (cm}^2/\text{s)}$  is the transverse diffusion and  $t \text{ (s)}$  is the drift time. Collectively, both longitudinal and transverse diffusion smear the distribution of deposited energy seen by each wire, thereby impacting the measured energy loss profile of a particle [24]. At the conditions expected for the SBND detector, the diffusion coefficients have been measured to be  $D_L = 7.2 \text{ cm}^2/\text{s}$  and  $D_T = 12.0 \text{ cm}^2/\text{s}$  [22].

In addition to diffusion, drifting electrons can also undergo attenuation. In this process, electrons are captured by electronegative impurities present in the liquid argon, most commonly oxygen and water [25]. This results in a reduction of electrons arriving at the wires, proportional to the drift distance. The number of charges collected on a wire  $Q_{wire}$  is typically modelled as an exponential suppression

$$Q_{Wire}(t) = Q_{Dep} \cdot \exp\left(\frac{-t}{\tau}\right) \quad (2.6)$$

where  $Q_{Dep}$  is the original number of deposited charges,  $t \text{ (ms)}$  is the drift time and  $\tau \text{ (ms)}$  is the electron lifetime characterising the level of charge attenuation. A high electron lifetime,

resulting from a low level of contamination, is a critical operational factor for achieving high efficiency in energy reconstruction. Recently reported from ProtoDUNE, which utilised the same membrane cryostat technology as SBND, the experiment measured a lifetime of  $\sim 10$  ms, equivalent to an oxygen purity of 3.4 ppt [25]. This lifetime is significantly larger than the drift time of SBND, which is projected to be 1.25 ms, making the effect of attenuation almost negligible.

A final important issue in electron transport is the so-called space charge effect (SCE). Argon ions, produced as part of the ionisation process, drift towards the cathode at a slower velocity than electrons. Typically, they have a drift velocity more than five orders of magnitude lower than that of electrons. [26]. Since SBND is a surface detector without an overburden, high exposure to cosmic rays leads to a high rate of ionisation. The resulting accumulation of slow-moving argon ions distorts the uniformity of the electric field, affecting both its intensity and direction. Fig. 2.8 illustrates the deformation of tracks drifting in the distorted electric field due to SCE. Track trajectories are impacted two-fold: bending away towards the detector edges as shown by the middle plot and bowing towards the cathode as shown by the right plot [27]. Moreover, distortions of the electric field also affect recombination previously discussed in Sec. 2.2.3, since the recombination factor is dependent on the electric field strength. Local fluctuations of recombination can subsequently impact the local charge yield resulting from an energy deposition.

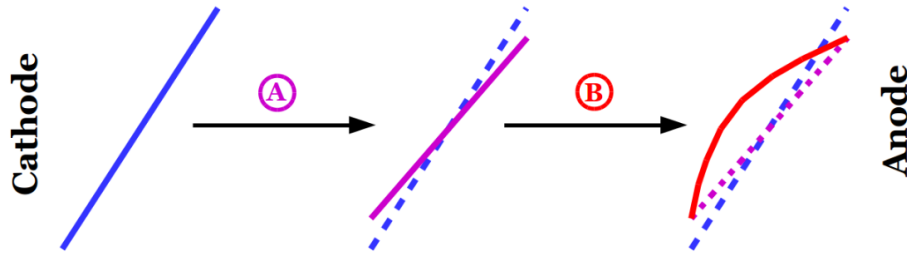


**Fig. 2.8** Schematic showing examples of the impact of SCE on tracks: bending away towards the detector edges (middle plot) and bowing towards the cathode (right plot) [27].

### 2.3.2 Photons Propagation

Scintillation photons can propagate over long distances in liquid argon since the medium is transparent to its own light. As scintillation photons travel, they undergo Rayleigh scattering as the first-order effect, involving the photons elastically scattering off atoms, altering their

trajectories. Reflections and refractions at the boundaries of the detector material are second-order effects. While these effects do not change the number of photons, they modify the paths of propagation and lengthen the travel time [28]. The impact of these effects on the probability of photons reaching the Photon Detection System (PDS) depends on the locations where the photons are created and their paths taken to arrive at the PDS. This consequently leads to a non-trivial distribution of photon arrival time at the PDS, and the travel time can range from a few to several tens of nanoseconds. Particularly, this effect is the most impactful on the prompt component of scintillation photons. The Rayleigh scattering length  $\lambda_{RS}$  for VUV photons in liquid argon has been reported to be around 50 cm [29] up to 110 cm [30], which is comparable to the size of SBND.

In addition to Rayleigh scattering, scintillation photons can also undergo absorption, which arises due to contaminants in liquid argon. Contaminants like nitrogen [31] and methane [32] have a high absorption cross section for VUV photons. Other contaminants, like oxygen and water, have also been observed in commercial argon and can also attenuate the number of photons [33]. The absorption of scintillation photons is modelled as an exponential suppression similar to Eq. 2.6 modelling the electron attenuation. The number of photons surviving absorption  $N_\gamma$  is as follows

$$N_\gamma(d) = N_0 \cdot \exp\left(\frac{-d}{\lambda_A}\right) \quad (2.7)$$

where  $N_0$  is the original number of scintillation photons,  $d$  is the propagation distance and  $\lambda_A$  the absorption length. Moreover, the absorption rate is dependent on the Rayleigh scattering length. Photons with a shorter  $\lambda_{RS}$  undergo longer and more indirect paths, increasing their probability of absorption before reaching the PDS [34].

Finally, an enhancement method for lighting collection efficiency in LArTPC is wavelength shifting scintillation photons. Specifically at SBND, TetraPhenyl Butadiene (TPB) is employed to shift the wavelength of VUV photon from 128 nm to 430 nm, which falls within the visible light range. This is to better match the detection spectrum of optical detectors installed at SBND [28], of which a description of the SBND PDS will be detailed in Chapter 3. Additionally, it provides extra handles for light reconstruction, of which the improvement will be discussed in Chapter 5.

The propagation characteristics of photons differ between the VUV and visible range. Fig. 2.9 shows the group velocity on the left and the Rayleigh scattering length on the right as a function of the photon wavelength in liquid argon. The vertical dashed blue and red lines at 128 and 430 nm respectively are the wavelengths of scintillation photons in liquid

argon and of photons re-emitted by TPB wavelength shifting. Here, it can be seen that the group velocity of VUV photons is slower than that of visible photons. Moreover, the Rayleigh scattering length of VUV photons is two orders of magnitude smaller compared to visible photons. This results in VUV photons being more susceptible to Rayleigh scattering and having a higher probability of absorption [34].

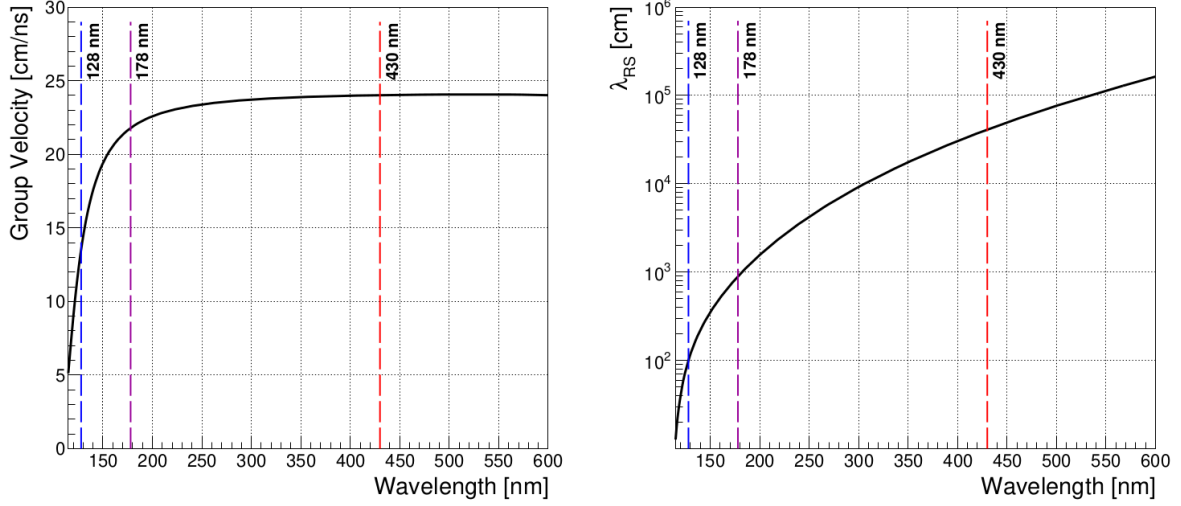


**Fig. 2.9** Plots showing the group velocity (left) and the Rayleigh scattering length (right) as a function of the photon wavelength in liquid argon [34].

## 2.4 Detection of Charge and Light

Upon arrival at the anode for detection, ionisation electrons and scintillation photons are read out by different detection technologies. Ionisation electron signals are recorded by the wire planes, which will be detailed in the following Sec. 2.4.1. Following that, Sec. 2.4.2 provides a description of two different types of optical detectors for detecting scintillation photons.

### 2.4.1 Wire Readouts

Once arrive at the anode, ionisation electrons induce signals on the wire plane readouts, which are made up of three planes separated by a few mm as previously depicted in Fig. 2.1. A bias voltage is applied to each wire plane to create a drift field across the three planes. This allows for electron transparency for the two innermost planes, also referred to as induction planes, where drifting electrons induce bipolar signals on the wires. The electrons are then

collected on the outermost plane, producing a unipolar signal, hence, this plane is referred to as the collection plane. Fig. 2.10 shows an example of induced currents on a wire as a function of time. Here, it can be seen a bipolar signal on an induction plane in red and a unipolar signal on a collection plane in blue. The three planes are oriented at an angle of  $60^\circ$  with respect to each other, of which the diagram in Fig. 2.1 shows three planes at the angle of  $0^\circ$  and  $\pm 60^\circ$  to the vertical. While three-dimensional spatial reconstruction of a signal requires a minimum of at least two wire planes, many modern LArTPC experiments use all three planes to improve the spatial resolution [6–9, 13, 25].

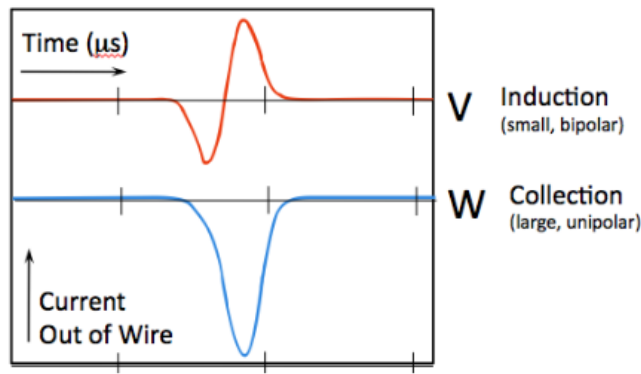


**Fig. 2.10** Plot showing current signals on the induction and collection wire plane induced by a point-like charge deposition [13].

The signals induced or collected on the wire planes are then shaped, amplified, and digitized before acquisition. Then, the measured signals are deconvolved for noise removal and the amount of charge collected is correlated with the energy deposited in the detector. Finally, the reconstruction of spatial and energy information is performed, which allows for high level analysis like particle identification. The reconstruction of charge signals at SBND will be further discussed in Chapter 5, Sec. 5.2.

### 2.4.2 Photomultiplier Tubes and X-ARAPUCAs

Scintillation photons are detected by the PDS located behind the wire planes, as depicted in Fig. 2.1. For SBND, which will be detailed in the forthcoming Chapter 3, the primary detection technology in the PDS is Photomultiplier Tubes (PMTs), which have a Quantum Efficiency (QE) of up to 30% [35]. However, PMTs are typically large and require sufficient volume inside the detector for installation. Current and future LArTPC experiments are increasingly adopting Silicon Photomultipliers (SiPMs) due to their advantageous smaller size, lower



power consumption, excellent signal-to-noise ratio, and a high QE of up to 40% [36]. The X-ARAPUCA device is a novel light collection technology utilising SiPMs, currently developed by Unicamp and being tested inside the SBND detector. Further description of X-ARAPUCA can be found in Ref. [37].

Both PMTs and X-ARAPUCAs are coated with wavelength shifting materials. The re-emitted light direction is isotropic, causing coated optical detectors to suffer a 50% reduction in efficiency due to photons being emitted away from the detection surface. PMTs are coated specifically with TPB, which can also impact the detection time as the emission of visible photons is not instantaneous. Multiple time components of re-emitted photons from TPB have been observed, with the majority of photons re-emitted within nanoseconds and a subset re-emitted as long as a few microseconds [38].

Photon signals measured by PMTs are digitized and acquired using a very high sampling frequency readout at the rate of 500 MHz [6]. This high sampling frequency gives the scintillation light signal much better timing resolution compared to the charge signal. As a result, it provides the most precise interaction timing information available in the detector. This is particularly important across different areas of the SBND detector. The PMT signals will be utilised for triggering which will be detailed in the forthcoming Chapter 3. In addition, the signals enable the timing resolution of the light reconstruction to reach the order of  $\mathcal{O}(1)$  ns, which will be covered in Chapter 5. Then, the timing performance of the DAQ to enable a stable and high frequency sampling of PMT signals will be further discussed in Chapter 6. All of these pave the way for the search for HNLs which is a key subject of this thesis, which will exploit the timing kinematic difference between HNL signals and SM neutrino backgrounds and will be covered in more detail in Chapter 8 and 9.

## 2.5 Concluding Remarks

Since originally proposed in 1977, the LArTPC concept has proven its potential for use in precision neutrino experiments. The understanding of particle interactions and their propagation within the detector, along with the detector's response to these particles, has significantly improved over time. Technological advancements in detection and readout now enable the scaling of LArTPCs from volumes of only several tons to even tens of kilotons, making them suitable for high multiplicity environments. This allows for the next generation of LArTPCs like the DUNE experiment to advance the field of neutrino physics. As described in the following Chapter 3, the SBND experiment and physics programme at Fermilab is a key part of this future.



## References

- [1] C. Rubbia, “The Liquid Argon Time Projection Chamber: A New Concept for Neutrino Detectors”, (1977).
- [2] J. N. Marx et al., “The Time Projection Chamber”, [Phys. Today](#) **31N10**, 46–53 (1978).
- [3] D. R. Nygren, “Origin and development of the TPC idea”, [Nuclear Instruments and Methods in Physics Research Section A: Accelerators, Spectrometers, Detectors and Associated Equipment](#) **907**, Advances in Instrumentation and Experimental Methods (Special Issue in Honour of Kai Siegbahn), 22–30 (2018).
- [4] W. Willis et al., “Liquid-argon ionization chambers as total-absorption detectors”, [Nuclear Instruments and Methods](#) **120**, 221–236 (1974).
- [5] P. A. Machado et al., “The Short-Baseline Neutrino Program at Fermilab”, [Annual Review of Nuclear and Particle Science](#) **69**, 363–387 (2019).
- [6] R. Acciarri et al. (SBND), “Construction of precision wire readout planes for the Short-Baseline Near Detector (SBND)”, [JINST](#) **15**, P06033 (2020).
- [7] R. Acciarri et al., “Design and construction of the MicroBooNE detector”, [Journal of Instrumentation](#) **12**, P02017 (2017).
- [8] S. Amerio et al. (ICARUS), “Design, construction and tests of the ICARUS T600 detector”, [Nucl. Instrum. Meth. A](#) **527**, 329–410 (2004).
- [9] B. Abi et al. (DUNE), “Deep Underground Neutrino Experiment (DUNE), Far Detector Technical Design Report, Volume IV: Far Detector Single-phase Technology”, [JINST](#) **15**, T08010 (2020).
- [10] R. S. Jones, “Muon-neutrino disappearance with multiple liquid argon time projection chambers in the Fermilab Booster neutrino beam”, PhD thesis (The University of Liverpool, 2021).
- [11] R. Acciarri et al. (MicroBooNE), “A Measurement of the Attenuation of Drifting Electrons in the MicroBooNE LArTPC”, [10.2172/1573054](#) (2017).
- [12] D. E. Groom et al., “Passage of particles through matter”, [The European Physical Journal C - Particles and Fields](#) **15**, 163–173 (2000).
- [13] C. Anderson et al., “The ArgoNeuT detector in the NuMI low-energy beam line at Fermilab”, [Journal of Instrumentation](#) **7**, P10019 (2012).
- [14] C. Adams et al. (MicroBooNE), “Reconstruction and measurement of  $\mathcal{O}(100)$  MeV energy electromagnetic activity from  $\pi_0 \rightarrow \gamma\gamma$  decays in the MicroBooNE LArTPC”, [Journal of Instrumentation](#) **15**, P02007 (2020).

- [15] R. Acciarri et al. (MicroBooNE), “Michel Electron Reconstruction Using Cosmic-Ray Data from the MicroBooNE LArTPC”, [JINST \*\*12\*\*, P09014 \(2017\)](#).
- [16] W. Foreman et al. (LArIAT Collaboration), “Calorimetry for low-energy electrons using charge and light in liquid argon”, [Phys. Rev. D \*\*101\*\*, 012010 \(2020\)](#).
- [17] A. Hitachi et al., “Effect of ionization density on the time dependence of luminescence from liquid argon and xenon”, [Phys. Rev. B \*\*27\*\*, 5279–5285 \(1983\)](#).
- [18] T. Doke et al., “Estimation of absolute photon yields in liquid argon and xenon for relativistic (1 MeV) electrons”, [Nucl. Instrum. Meth. A \*\*291\*\*, 617–620 \(1990\)](#).
- [19] T. Doke et al., “Absolute Scintillation Yields in Liquid Argon and Xenon for Various Particles”, [Jap. J. Appl. Phys. \*\*41\*\*, 1538–1545 \(2002\)](#).
- [20] R. Acciarri et al., “A study of electron recombination using highly ionizing particles in the ArgoNeuT Liquid Argon TPC”, [Journal of Instrumentation \*\*8\*\*, P08005 \(2013\)](#).
- [21] S. Kubota et al., “Dynamical behavior of free electrons in the recombination process in liquid argon, krypton, and xenon”, [Phys. Rev. B \*\*20\*\*, 3486–3496 \(1979\)](#).
- [22] Y. Li et al., “Measurement of longitudinal electron diffusion in liquid argon”, [Nuclear Instruments and Methods in Physics Research Section A: Accelerators, Spectrometers, Detectors and Associated Equipment \*\*816\*\*, 160–170 \(2016\)](#).
- [23] P. Abratenko et al. (MicroBooNE), “Measurement of the longitudinal diffusion of ionization electrons in the MicroBooNE detector”, [Journal of Instrumentation \*\*16\*\*, P09025 \(2021\)](#).
- [24] G. Putnam et al., “Effect of diffusion on the peak value of energy loss observed in a LArTPC”, [JINST \*\*17\*\*, P10044 \(2022\)](#).
- [25] B. Abi et al., “First results on ProtoDUNE-SP liquid argon time projection chamber performance from a beam test at the CERN Neutrino Platform”, [Journal of Instrumentation \*\*15\*\*, P12004 \(2020\)](#).
- [26] M. Antonello et al., “Study of space charge in the ICARUS T600 detector”, [Journal of Instrumentation \*\*15\*\*, P07001 \(2020\)](#).
- [27] M. Mooney, “The MicroBooNE Experiment and the Impact of Space Charge Effects”, in Meeting of the APS Division of Particles and Fields (Nov. 2015).
- [28] P. Abratenko et al. (SBND), “Scintillation Light in SBND: Simulation, Reconstruction, and Expected Performance of the Photon Detection System”, (2024).
- [29] E. Grace et al., “Index of refraction, Rayleigh scattering length, and Sellmeier coefficients in solid and liquid argon and xenon”, [Nucl. Instrum. Meth. A \*\*867\*\*, 204–208 \(2017\)](#).
- [30] M. Babicz et al., “A measurement of the group velocity of scintillation light in liquid argon”, [JINST \*\*15\*\*, P09009 \(2020\)](#).
- [31] B. J. P. Jones et al., “A Measurement of the Absorption of Liquid Argon Scintillation Light by Dissolved Nitrogen at the Part-Per-Million Level”, [JINST \*\*8\*\*, \[Erratum: JINST \*\*8\*\*, E09001 \(2013\)\], P07011 \(2013\)](#).
- [32] B. J. P. Jones et al., “The Effects of Dissolved Methane upon Liquid Argon Scintillation Light”, [JINST \*\*8\*\*, P12015 \(2013\)](#).

## References

---

- [33] J. Calvo et al. (ArDM), “Measurement of the attenuation length of argon scintillation light in the ArDM LAr TPC”, [Astropart. Phys. \*\*97\*\*, 186–196 \(2018\)](#).
- [34] P. J. Green, “Light and Dark in Liquid argon time Projection Chamber Neutrino Detectors”, PhD thesis (The University of Manchester, 2022).
- [35] R. Acciarri et al., “Demonstration and Comparison of Operation of Photomultiplier Tubes at Liquid Argon Temperature”, [JINST \*\*7\*\*, P01016 \(2012\)](#).
- [36] A. Gola et al., “Nuv-sensitive silicon photomultiplier technologies developed at fondazione bruno kessler”, [Sensors \*\*19\*\*, 10.3390/s19020308 \(2019\)](#).
- [37] E. Segreto et al., “First liquid argon test of the x-arapuca”, [Journal of Instrumentation \*\*15\*\*, C05045 \(2020\)](#).
- [38] E. Segreto, “Evidence of delayed light emission of TetraPhenyl Butadiene excited by liquid Argon scintillation light”, [Phys. Rev. C \*\*91\*\*, 035503 \(2015\)](#).